Diagnosing the thickness-weighted averaged eddy-mean flow interaction in an eddying North Atlantic ensemble

Takaya Uchida[1*], Quentin Jamet[1], William Dewar[1,2], Dhruv Balwada[3], Julien Le Sommer[1]& Thierry Penduff[1]

[1]Institut des Géosciences de l'Environnement, Centre National de la Recherche Scientifique, France

[2]Department of Earth, Ocean and Atmospheric Science, Florida State University, USA

[3]School of Oceanography, University of Washington, USA

Key Points:

- Mesoscale-resolving ensemble runs of the North Atlantic Ocean are used to diagnose the thickness-weighted averaged eddy-mean flow interaction.
- The Eliassen-Palm flux divergence, which is directly related to the eddy Ertel potential vorticity (PV) flux, tends to meridionally decelerate the Gulf Stream.
- The eddy Ertel PV flux can be parametrized as a local-gradient flux of the residual-mean Ertel PV via an anisotropic eddy diffusivity tensor.

*

Corresponding author: Takaya Uchida, `takaya.uchida@univ-grenoble-alpes.fr`

Abstract

The thickness-weighted average (TWA) framework, which treats the residual-mean flow as the prognostic variable, has provided us with a clear theoretical understanding of the eddy feedback onto the residual-mean flow. The averaging operator involved in the TWA framework, although in theory being an ensemble mean, in practice has often been approximated by a temporal mean, which conflates the temporal variability with the eddies. Here, we analyze an ensemble of North Atlantic simulations at mesoscale resolving resolution (1/12°). We therefore recognize means and eddies in terms of ensemble means and fluctuations about those means, in keeping with the TWA formalism proposed by Young (2012). Eddy-mean flow feedbacks are encapsulated in the Eliassen-Palm (E-P) flux tensor and its divergence indicates that the eddies contribute to the zonal meandering of the Gulf Stream and its deceleration in the meridional direction. We also show that the eddy Ertel potential vorticity (PV) flux can be parametrized as an isopycnic local-gradient flux of the residual-mean Ertel PV via an anisotropic eddy diffusivity tensor. As the E-P flux divergence and eddy Ertel PV flux are directly related to one another, this provides a new pathway forward for a unified mesoscale eddy closure scheme.

Plain Language Summary

We have greatly benefited from global climate simulations in gaining insight into what the climate would look like in an ever warming future. Due to computational constraints, however, the oceanic component of such simulations have been poorly constrained; the storm systems in the ocean, often referred to as eddies, have the spatial scales of roughly 50 km and simulating this accurately on a global scale, which is on the order of 1000 km, has remained challenging. Although relatively small in scale compared to the global Earth, eddies have been known to modulate the climate by transporting heat from the equator to the poles. By running a regional simulation of the North Atlantic Ocean and taking advantage of recent theoretical development, we provide a new pathway in improving the representation of these eddies and as such, improving global ocean and climate simulations.

1 Introduction

Eddy-mean flow interaction has been a key framework in understanding jet formation in geophysical flows such as in the atmosphere and ocean (e.g. Vallis, 2017, Chapters 12 and 15). A prominent example of such a jet in the North Atlantic ocean is the Gulf Stream. Previous studies have shown how eddies fluxing buoyancy and momentum back into the mean flow energize the Gulf Stream (Lévy et al., 2010; Waterman & Lilly, 2015; Chassignet & Xu, 2017; Aluie et al., 2018). Basin-scale simulations, however, often lack sufficient spatial resolution to accurately resolve the eddies and hence, result in underestimating the eddy fluxes of momentum and tracers (Capet et al., 2008; Arbic et al., 2013; Kjellsson & Zanna, 2017; Balwada et al., 2018; Uchida et al., 2019; Schubert et al., 2020). Due to computational constraints, we will continue to rely on models which only partially resolve the mesoscale, a scale roughly on the order of O(20-200 km) at which the ocean currents are most energetic (Stammer, 1997; Xu & Fu, 2011, 2012; Ajayi et al., 2020), for global ocean and climate simulations. As a result, there has been an ongoing effort to develop energy-backscattering eddy parametrizations which incorporate the dynamical effects of eddy momentum fluxes due to otherwise unresolved mesoscale turbulence (e.g. Kitsios et al., 2013; Anstey & Zanna, 2017; Zanna & Bolton, 2020; Bachman et al., 2018; Bachman, 2019; Jansen et al., 2019; Perezhogin, 2019; Juricke et al., 2020).

There has been less emphasis, however, on quantifying the spatial and temporal characteristics of the eddy buoyancy and momentum fluxes themselves, which the parametrizations are deemed to represent. The focus of this study is, therefore, to examine the dynamical effects of mesoscale turbulence on the mean flow in realistic partially air-sea coupled eddying ensemble runs of the North Atlantic. To achieve this goal, we employ the thickness-weighted average (TWA) framework developed by De Szoeke and Bennett (1993), Young (2012), J. R. Maddison and Marshall (2013) and Aoki (2014), which treats the residual-mean velocity as a prognostic variable and allows for a straightforward theoretical understanding of the eddy feedback onto the (residual) mean flow; the framework has been fruitful in examining eddy-mean flow interaction in idealized modelling studies (e.g. D. P. Marshall et al., 2012; Cessi & Wolfe, 2013; Ringler et al., 2017; Bire & Wolfe, 2018).

To our knowledge, Aiki and Richards (2008), Aoki et al. (2016) and Zhao and Marshall (2020) are the only studies that diagnose the TWA framework in realistic ocean simulations. Aiki and Richards (2008), however, recompute the hydrostatic pressure using potential density for their off-line diagnosis in defining their buoyancy coordinate, which can result in significant discrepancies from the pressure field used in their on-line calculation and consequently errors in the diagnosed geostrophic shear. Aoki et al. (2016) negate this complication between the buoyancy coordinate and pressure field by analyzing their outputs in geopotential coordinates but with the limitation of second-order accuracy in eddy fluxes, and all three studies assume ergodicity. The ergodic assumption of treating a temporal mean equivalent to an ensemble mean, although a pragmatic one, prevents examining the temporal evolution of the residual mean fields and conflates temporal variability with the eddies, which can have leading-order consequences in quantifying the energy cycle (c.f. Aiki & Richards, 2008, Table 2 in their paper); by adjusting the temporal mean from monthly to annual, they show that the amount of kinetic and potential energy stored in the mean and eddy reservoirs can change up to a factor of four. Eddy-mean flow interaction in the TWA framework, hence, warrants further investigation, and we believe our study is the first to strictly implement an ensemble mean in this context.

When discussing *eddy* versus *mean flow*, one of the ambiguities lies in how the two are decomposed (Bachman et al., 2015). As noted above, often, the eddies are defined from a practical standpoint as the deviation from a temporally and/or spatially coarse-grained field regardless of the coordinate system (e.g. Aiki & Richards, 2008; Lévy et al., 2012; Sasaki et al., 2014; Griffies et al., 2015; Aoki et al., 2016; Uchida et al., 2017; Zhao & Marshall, 2020), which leaves open the question of how the filter affects the decomposition. Due to the ensemble averaging nature of the TWA framework, we are uniquely able to define the two; the *mean flow* (ensemble mean) is the predictable field determined by the surface boundary forcings and the *eddy* (residual from the ensemble mean) the field due to intrinsic variability of mesoscale turbulence (Sérazin et al., 2017; Leroux et al., 2018).

The paper is organized as follows: We describe the model configuration in section 2 and briefly provide an overview of the TWA framework in section 3. The results are given in section 4. In particular, we highlight in section 4.2 how the Eliassen-Palm (E-P) flux divergence is related to the Ertel potential vorticity (PV) and that it can be parametrized via a local-gradient flux closure. Discussion and conclusions are given in section 5.

2 Model description

The model configuration is similar to the realistic air-sea coupled runs in Jamet et al. (2019a); Jamet et al. (2019b) and Jamet et al. (2020) where we run 12 air-sea partially coupled ensemble members of the North Atlantic ocean at mesoscale resolving resolution (1/12°) using the hydrostatic configuration of the Massachusetts Institute of Technology general circulation model (MITgcm; J. Marshall et al., 1997). We have 46 vertical levels increasing from 6 m near the surface to 250 m at depth. Harmonic, biharmonic horizontal and vertical viscosity values of $A_{\mathrm{h2}} = 20$ m^2 s^{-1}, $A_{\mathrm{h4}} = 10^{10}$ m^4 s^{-1} and $A_{\mathrm{v}} = 10^{-5}$ m^2 s^{-1} were used respectively. For completeness, we provide a brief summary of the configuration below.

Figure 1 shows the bathymetry of the modelled domain extending from 20°S to 55°N. In order to save computational time and memory allocation, the North Atlantic basin was configured to zonally wrap around periodically. Open boundary conditions are applied at the north and south boundaries of our domain and Strait of Gibraltar, such that oceanic velocities ($\mathbf{u}$) and tracers (θ, s) are restored with a 36 minutes relaxation time scale toward a state derived by an ocean-only global Nucleus for European Modelling of the Ocean (NEMO) simulation (Molines et al., 2014, ORCA12.L46-MJM88 run in their paper). A sponge layer is applied to the two adjacent grid points at the open boundaries where model variables are restored toward boundary conditions with a one-day relaxation time scale. Although relatively short, no adverse effects were apparent upon inspection in response to these relaxation time scales (not shown). The open boundary conditions are applied every five days and linearly interpolated in between.

The 12-member ensemble was constructed as follows: From a simulation run under yearly repeating atmospheric forcing and boundary conditions taken from the (Jamet et al., 2020, Open boundary conditions Climatologic and Atmosphere Climatologic (OCAC) ensemble runs in their paper), 12 snapshots of the OCAC model state with a four-year interval between each are selected and used to initialise each ensemble member used in this study. Such initial conditions are meant to reflect the growth of dynamically consistent oceanic perturbations de-correlated at both seasonal and interannual time scales; they are usually referred to as macro initial conditions (Stainforth et al., 2007; Hawkins et al., 2016). At the surface, the ocean is partially coupled to an atmospheric boundary layer model (CheapAML; Deremble et al., 2013). In CheapAML, atmospheric surface

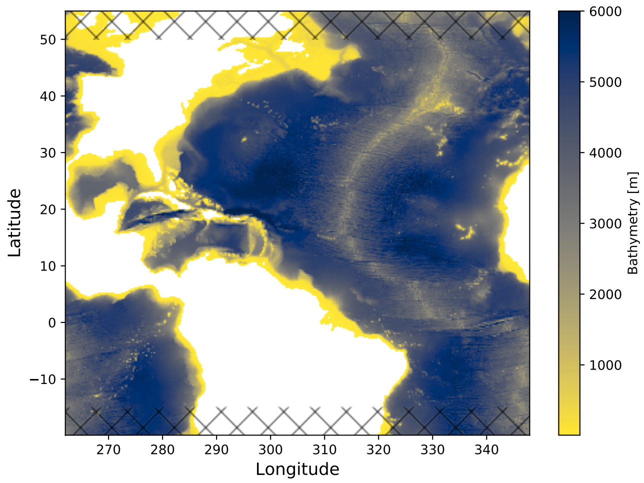

Figure 1. Bathymetry of the modelled domain. The domain is configured to wrap around zonally. The hatches indicate the northern and southern regions excluded from our analysis.

temperature and relative humidity respond to ocean surface structures by exchanges of heat and humidity computed according to the Coupled Ocean–Atmosphere Response Experiment (COARE3; Fairall et al., 2003) flux formula, but are strongly restored toward prescribed values over land; there are no zonally propagating signals of climate teleconnection. The 12 ensemble members are then integrated forward in time for five years (1963-1967), and exposed to the same realistic forcing across all ensemble members; the surface forcing is taken from the Drakkar forcing set and boundary forcing from the ORCA12.L46-MJM88 run (details are given in Jamet et al., 2019a). During this interval, the oceanic state and the atmospheric boundary layer temperature and humidity evolve in time. In the following, we interpret the ensemble mean as the ocean response to the prescribed atmospheric forcing, while the ensemble spread is attributed to intrinsic ocean dynamics that develop at mesoscale-resolving resolution (Sérazin et al., 2017; Leroux et al., 2018; Jamet et al., 2019b).

The model outputs were saved as instantaneous snapshots every five days and five-day averages. We examined whether the five-day temporal smoothing would affect the terms in the E-P flux described below, upon which we found the difference between the eddy-eddy correlation terms diagnosed from instantaneous and temporally averaged fields to be up to same order of the total variance of the instantaneous field (not shown). The additional dimension of ensembles also negates the necessity for any temporal averaging to define the mean. As such, in the following analysis, we will only use the instantaneous snapshot outputs. We also exclude the northern and southern extent of 5° and first year of integration from our analysis to avoid effects from the open boundary conditions, sponge layer and initialization shock, and to maximize the intrinsic variability amongst the ensemble members respectively.

3 Theory and implementation of thickness-weighted averaging

The ocean is a stratified fluid, and the circulation and advection of tracers tend to align themselves along the stratified density surfaces. Hence, the most natural way to understand the circulation is to consider the variables in a thickness-weighted form and the residual-mean flow rather than the Eulerian mean flow. We leave the detailed derivation of the TWA framework to Young (2012) and here, only provide a brief summary; the primitive equations in geopotential coordinates are first transformed to buoyancy coordinates upon which a thickness weighting and ensemble averaging along constant buoyancy surfaces is applied to obtain the TWA governing equations. Following Young's notation, the TWA horizontal momentum equations in the buoyancy coordinate system $(\tilde{t}, \tilde{x}, \tilde{y}, \tilde{b})$ are:

$$\hat{u}_{\tilde{t}} + \hat{u}\hat{u}_{\tilde{x}} + \hat{v}\hat{u}_{\tilde{y}} + \hat{\varpi}\hat{u}_{\tilde{b}} - f\hat{v} + \overline{m}_{\tilde{x}} = -\overline{\mathbf{e}}_1 \cdot (\nabla \cdot \mathbf{E}) + \hat{\mathcal{X}} \tag{1}$$

$$\hat{v}_{\tilde{t}} + \hat{u}\hat{v}_{\tilde{x}} + \hat{v}\hat{v}_{\tilde{y}} + \hat{\varpi}\hat{v}_{\tilde{b}} + f\hat{u} + \overline{m}_{\tilde{y}} = -\overline{\mathbf{e}}_2 \cdot (\nabla \cdot \mathbf{E}) + \hat{\mathcal{Y}} \tag{2}$$

where $\widehat{(\cdot)}$ and $\overline{(\cdot)}$ are the TWA and ensemble-mean variables respectively and the subscripts denote partial derivatives. The Montgomery potential is $m = \phi - \tilde{b}\zeta$ where ϕ is the dynamically active part of hydrostatic pressure and ζ is the isopycnal depth. The vectors $\overline{\mathbf{e}}_1 = \mathbf{i} + \overline{\zeta}_{\tilde{x}}\mathbf{k}$ and $\overline{\mathbf{e}}_2 = \mathbf{j} + \overline{\zeta}_{\tilde{y}}\mathbf{k}$ form the basis vectors spanning the buoyancy horizontal space where $\mathbf{i}$, $\mathbf{j}$ and $\mathbf{k}$ are the Cartesian geopotential unit vectors (Young, 2012; Ringler et al., 2017), and $\mathbf{E}$ is the E-P flux tensor described in detail in Section 4.1. $\mathcal{X}$ and $\mathcal{Y}$ are the viscous and forcing terms.

One subtle yet important point involves the buoyancy coordinate $(\tilde{b})$ for a realistic, non-linear equation of state (EOS) for density (Jackett & Mcdougall, 1995). The analysis in Young (2012) implicitly assumes a linear EOS. With a realistic EOS the vertical coordinate can no longer "naively" be defined by neutrally-surfaced isopycnals which allow for adiabatic adjustment, such as potential density, and is the subject of some debate. We argue for the use of in-situ density (detailed arguments are given in Appendix A); other choices can be made (e.g. Stanley, 2019). The consequence of using in-situ buoyancy as the coordinate ($\tilde{b} = -g(\rho-\rho_0)/\rho_0$ where ρ is the in-situ density and $\rho_0 = 999.8$ kg m^{-3} is the Boussinesq reference density) is that buoyancy is no longer conserved due to compressibility effects even under adiabatic conditions, i.e.

$$\frac{D\tilde{b}}{Dt} = \frac{wg^2}{c_s^2} \tag{3}$$

where c_s is the speed of sound and the vertical velocity is $w = \frac{D\zeta}{Dt}$. The right-hand side of eqn. (3) can be included with the diapycnal velocity $\varpi = \tilde{b}_\theta\dot{\theta} + \tilde{b}_s\dot{s} - \tilde{b}_\Phi\rho_0 wg$ where $\dot{\theta}$ and $\dot{s}$ are the net diabatic contributions on potential temperature and practical salinity respectively calculated online and outputted as diagnostics, and $\tilde{b}_\Phi \overset{\text{def}}{=} -\frac{g}{\rho_0 c_s^2}$ is the compressibility effect due to the dynamically non-active part of the hydrostatic pressure. The use of in-situ buoyancy maintains the desirable properties of a unique, statically stable vertical coordinate, a simple hydrostatic balance ($\sigma = \zeta_{\tilde{b}} = -m_{\tilde{b}\tilde{b}}$), the impermeability of Ertel PV ($\Pi = \sigma^{-1}(f + v_{\tilde{x}} - u_{\tilde{y}})$) and nonacceleration conditions (Young, 2012) with a correction due to compressibility (the pressure term in ϖ). Discussion regarding the energetics are given in Appendix B.

The raw simulation outputs were in geopotential coordinates so we first remapped all of the variables in eqns. (1) and (2) onto 60 buoyancy levels spread linearly across the range of $\tilde{b} \in [-0.196, -0.491]$ [m s^{-2}]:

$$(\mathbf{u}, z, \nabla_{\rm h}\phi, \theta, s, \rho_\theta\dot{\theta}, \rho_s\dot{s}, \frac{wg^2}{c_s^2})(t, x, y, z) \longmapsto (\mathbf{u}, \zeta, \tilde{\nabla}_{\rm h} m, \theta, s, \rho_\theta\dot{\theta}, \rho_s\dot{s}, \frac{wg^2}{c_s^2})(\tilde{t}, \tilde{x}, \tilde{y}, \tilde{b}) \tag{4}$$

using the `fastjmd95` Python package to compute the in-situ density and its partial derivatives (Abernathey, 2020), and the `xlayers` Python package (Jones, 2019; Jones et al., 2020) which implements the MITgcm layers package off-line and allows for coordinate remapping consistent with the finite-volume discretization. For the horizontal pressure gradient, we have invoked the identity:

$$\nabla_{\rm h}\phi(z) \longmapsto \nabla_{\rm h}\phi(\tilde{b}) = \tilde{\nabla}_{\rm h} m \tag{5}$$

where the subscript $(\cdot)_{\rm h}$ represents the horizontal gradient and $\tilde{\nabla}_{\rm h} = (\partial_{\tilde{x}}, \partial_{\tilde{y}})$. Note identity (5) only holds when in-situ buoyancy is used as the coordinate system, see eqns. (A1-A3).

4 Results

We start by showing the time series of domain-averaged horizontal kinetic energy (KE) and potential temperature (Fig. 2a). The OCAC run, from which the initial conditions were taken, had a long-term warming trend so we corrected for this in our offline analysis by removing the domain-integrated residual heat content from the ensemble mean at the initial time step defined as:

$$\Delta\theta_i \stackrel{\text{def}}{=} \frac{\int C_p(\theta_i - \overline{\theta})dV}{\int C_p dV} \tag{6}$$

where the subscript i ($= [1, 2, \dots, 12]$) is the ensemble index and $C_p = 3929.245$ J kg^{-1} K^{-1} is the specific heat capacity (McDougall, 2003); the residual per ensemble member ($\Delta\theta_i$) was removed from the potential temperature throughout the five years of output prior to the following analysis. We also corrected for salinity in the same manner. Figure 2a shows the simulation has a prominent seasonal cycle with a slight cooling trend and increase in KE.

In Fig. 2, we also show the (residual) mean fields on December 26, 1963, the last day of the spin-up period. The depth of the buoyancy level shown in Fig. 2c is below the ensemble-mean mixed-layer depth (MLD; Fig. 2b) basin wide where diabatic effects are small. We focus on this buoyancy level for the remainder of this study as it is below the MLD and the isopycnal does not outcrop but is shallow enough to capture the imprint of the Gulf Stream and eddies. The ensemble-mean MLD was computed as the depth at which the potential density computed from ensemble-mean temperature and salinity fields increased by 0.03 kg m^{-3} from the density at 10 m depth ($\overline{\text{MLD}} \stackrel{\text{def}}{=} \text{MLD}(\overline{\theta}, \overline{s})$; de Boyer Montégut et al., 2004). The mean KE fields ($K^{\#} \stackrel{\text{def}}{=} |\hat{\mathbf{u}}|^2/2$; Fig. 2d) show the characteristic features of the Gulf Stream, North Brazil Current and equatorial undercurrent. The mean Rossby number ($\text{Ro}^{\#} \stackrel{\text{def}}{=} f^{-1}(\hat{v}_{\tilde{x}} - \hat{u}_{\tilde{y}})$) shown in Fig. 2e is smaller than unity except for near the equator where the Coriolis parameter becomes small, indicating that over most of the North Atlantic basin, the mean flow in the interior is balanced. The kinematics of discretizing the gradients in buoyancy coordinates are given in Appendix C. We now move on to examine the eddy feedback onto the mean flow.

4.1 The Eliassen-Palm flux tensor

The E-P flux tensor ($\mathbf{E}$) in the TWA framework (eqns. (1) and (2)) is:

$$\mathbf{E} = \begin{pmatrix} \widehat{u''u''} + \frac{1}{2\overline{\sigma}}\overline{\zeta'^2} & \widehat{u''v''} & 0 \\ \widehat{v''u''} & \widehat{v''v''} + \frac{1}{2\overline{\sigma}}\overline{\zeta'^2} & 0 \\ \widehat{\varpi''u''} + \frac{1}{\overline{\sigma}}\overline{\zeta' m'_{\tilde{x}}} & \widehat{\varpi''v''} + \frac{1}{\overline{\sigma}}\overline{\zeta' m'_{\tilde{y}}} & 0 \end{pmatrix} \tag{7}$$

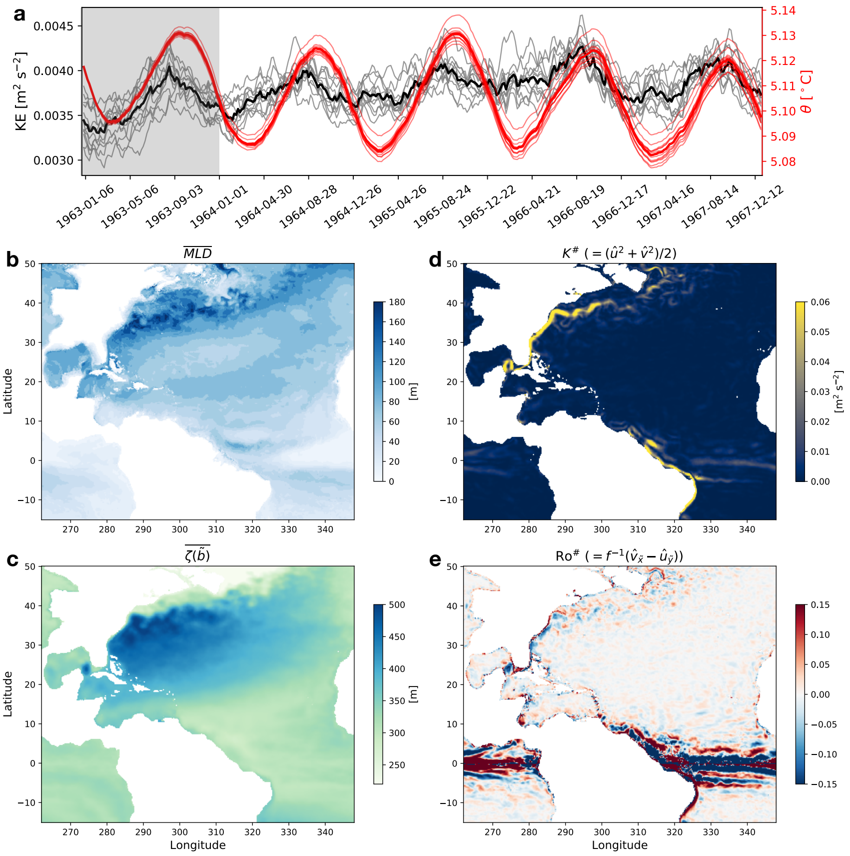

Figure 2. Time series of the domain-averaged KE (black) and temperature corrected for its residual heat content (red) for the 12 ensemble members between 15S-50N. The thick lines represent the ensemble mean and the grey shading indicates the one-year spin up period **a**. **b**,**c** The ensemble-mean MLD on December 26, 1963 and isopycnal depth with the buoyancy $\tilde{b} = -0.276$ [m s^{-2}]. **d**,**e** The TWA kinetic energy ($K^{\#}$) and Rossby number (Ro$^{\#}$) on the isopycnal.

where $(\cdot)'' = (\cdot) - \widehat{(\cdot)}$ and $(\cdot)' = (\cdot) - \overline{(\cdot)}$ are the residual of instantaneous snapshot outputs from the thickness-weighted and ensemble averages respectively (J. R. Maddison & Marshall, 2013; Aoki, 2014; Ringler et al., 2017). The two are related via the quasi-Stokes velocity (Greatbatch, 1998; McDougall & McIntosh, 2001):

$$\begin{aligned}\mathbf{u}'' &= \mathbf{u} - \frac{\overline{\mathbf{u}\sigma}}{\overline{\sigma}} = \overline{\mathbf{u}} + \mathbf{u}' - \frac{\overline{(\overline{\mathbf{u}} + \mathbf{u}')(\overline{\sigma} + \sigma')}}{\overline{\sigma}} \\ &= \mathbf{u}' + \frac{\overline{\mathbf{u}'\sigma'}}{\overline{\sigma}}.\end{aligned}$$

We show each term in eqn. (7) in Fig. 3. The Reynolds stress term $\widehat{u''v''}$ is associated with barotropic processes (e.g. Vallis, 2017, Chapter 15). The eddy momentum flux terms $\widehat{|\mathbf{u}''|^2}$ in Fig. 3b,e are seen to exchange momentum between eddies and the mean flow, i.e. to accelerate or decelerate the Gulf Stream. The interfacial form stress ($\overline{\zeta'\tilde{\nabla}_{\mathrm{h}} m'}$; Fig. 3c,f) associated with baroclinic instability is "deceivingly" orders of magnitude smaller than the other terms. The contribution from the adiabatic and compressibility effects (i.e. the terms with ϖ) were smaller than the interfacial form stress by another order of magnitude or more in the subtropics (not shown). It is important to keep in mind, however, that it is the divergence of the E-P flux and not the flux itself that goes into the momentum equation, and the horizontal ($\tilde{\nabla}_{\mathrm{h}}$) and vertical gradient ($\partial_{\tilde{b}}$) differ by roughly $\mathrm{O}(10^6)$.

Writing out the E-P flux divergence in eqns. (1) and (2) gives:

$$\begin{aligned}-\overline{\mathbf{e}}_1 \cdot (\tilde{\nabla} \cdot \mathbf{E}) &= -\overline{\sigma}^{-1}\Big(\big[\overline{\sigma}(\widehat{u''u''} + \frac{1}{2\overline{\sigma}}\overline{\zeta'^2})\big]_{\tilde{x}} + \big[\overline{\sigma}\widehat{v''u''}\big]_{\tilde{y}} + \big[\overline{\sigma}(\widehat{\varpi''u''} + \frac{1}{\overline{\sigma}}\overline{\zeta' m'_{\tilde{x}}})\big]_{\tilde{b}}\Big) \qquad (8) \\ &= -\overline{\sigma}^{-1}\Big([\overline{\sigma u''u''} + \overline{\zeta'^2}/2]_{\tilde{x}} + [\overline{\sigma v''u''}]_{\tilde{y}} + [\overline{\sigma\varpi''u''} + \overline{\zeta' m'_{\tilde{x}}}]_{\tilde{b}}\Big), \qquad (9)\end{aligned}$$

$$\begin{aligned}-\overline{\mathbf{e}}_2 \cdot (\tilde{\nabla} \cdot \mathbf{E}) &= -\overline{\sigma}^{-1}\Big(\big[\overline{\sigma}\widehat{u''v''}\big]_{\tilde{x}} + \big[\overline{\sigma}(\widehat{v''v''} + \frac{1}{2\overline{\sigma}}\overline{\zeta'^2})\big]_{\tilde{y}} + \big[\overline{\sigma}(\widehat{\varpi''v''} + \frac{1}{\overline{\sigma}}\overline{\zeta' m'_{\tilde{y}}})\big]_{\tilde{b}}\Big) \qquad (10) \\ &= -\overline{\sigma}^{-1}\Big([\overline{\sigma u''v''}]_{\tilde{x}} + [\overline{\sigma v''v''} + \overline{\zeta'^2}/2]_{\tilde{y}} + [\overline{\sigma\varpi''v''} + \overline{\zeta' m'_{\tilde{y}}}]_{\tilde{b}}\Big). \qquad (11)\end{aligned}$$

Figure 4 shows that the divergence of interfacial form stress becomes a leading-order term along with the eddy momentum fluxes in the Gulf Stream region. The magnitude of the divergence of Reynolds stress term attributable to barotropic instability is the smallest (Fig. 4b,e). In the North Brazil Current region, the signal of baroclinic instability is insignificant (Fig. 4c,g) relative to barotropic instability and eddy momentum fluxes (Fig. 4a,b,e,f). It is quite surprising that the signal of the equatorial undercurrents, although having high KE (Fig. 2d), is significantly smaller than in the Gulf Stream and North Brazil Current regions, virtually not visible in Figs. 3 and 4. This implies that the residual-mean flow dominates over the eddies in the equatorial region.

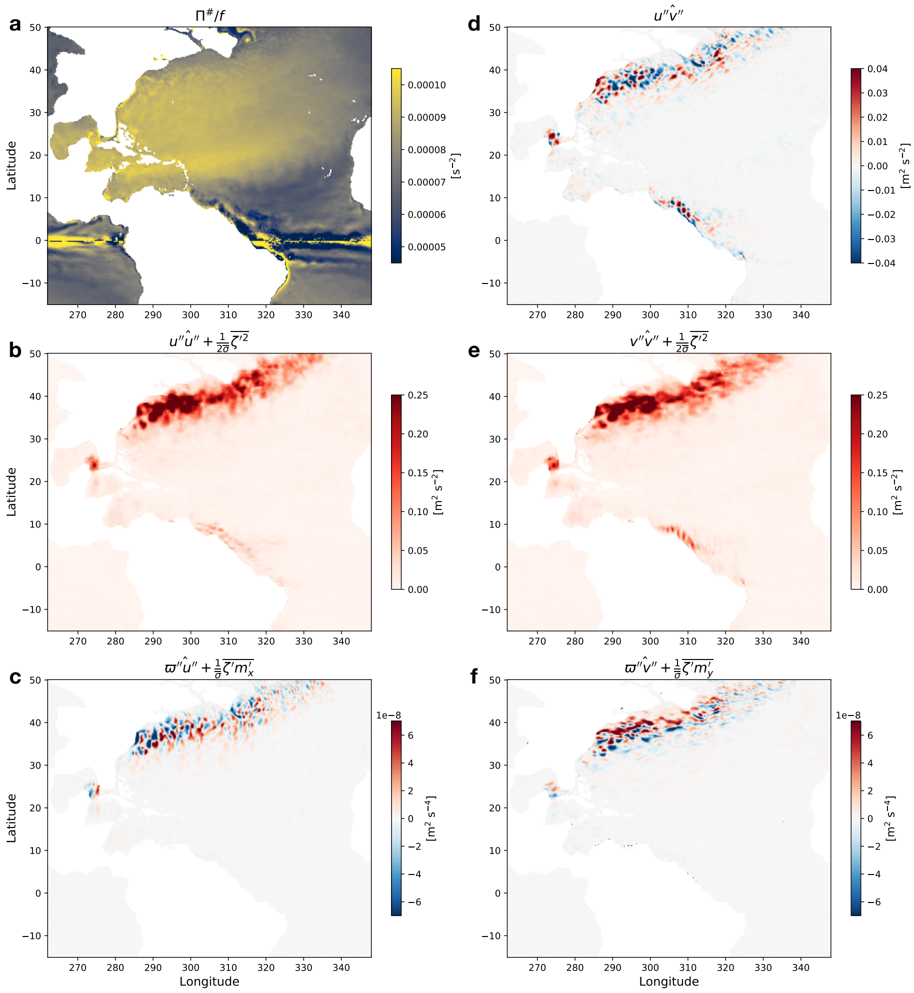

Figure 3. The residual-mean Ertel potential vorticity normalized by the local Coriolis parameter ($\Pi^\#/f \overset{\text{def}}{=} \overline{\sigma}^{-1}(1 + \text{Ro}^\#)$) **a** and terms in the E-P flux tensor **b-f** on December 26, 1963 on the isopycnal layer as in Fig. 2.

We now examine further details in the Gulf Stream region. The dipole features in the zonal direction of Reynolds stress and interfacial form stress likely contribute to the jet meandering (Fig. 4a,c). In the meridional direction, the eddy momentum flux divergence tends to smooth out the Gulf Stream (accelerate the Gulf Stream on the northern flank and decelerate it on the southern flank; Fig. 4f), while the divergence of interfacial form stress (i.e. baroclinic instability) counteracts to sharpen it (Fig. 4g). The divergence of the eddy momentum fluxes and interfacial form stress largely cancel each other out (Fig. 4a,c,f,g), however, with the residual generally having dipole features in the zonal direction (Fig. 4d), and fluxing momentum out of the mean flow in the meridional direction (Fig. 4h). This net zonal dipole feature and meridional deceleration of the Gulf Stream were the case for any randomly chosen day in our five years of ensembles (not shown).

4.2 The Ertel potential vorticity flux

As was noted by Young (2012), the E-P flux divergence is directly related to the eddy Ertel PV flux and can be written as:

$$\overline{\mathbf{e}}_1 \cdot (\tilde{\nabla} \cdot \mathbf{E}) = -\overline{\sigma}\widehat{\mathbf{u}''\Pi^\star} \cdot \mathbf{j} \ , \quad \overline{\mathbf{e}}_2 \cdot (\tilde{\nabla} \cdot \mathbf{E}) = \overline{\sigma}\widehat{\mathbf{u}''\Pi^\star} \cdot \mathbf{i} \ , \tag{12}$$

where $\widehat{\mathbf{u}''\Pi^\star} \overset{\text{def}}{=} \overline{\sigma}^{-1}\big[\{\overline{\mathbf{e}}_2 \cdot (\tilde{\nabla} \cdot \mathbf{E})\}\overline{\mathbf{e}}_1 - \{\overline{\mathbf{e}}_1 \cdot (\tilde{\nabla} \cdot \mathbf{E})\}\overline{\mathbf{e}}_2\big]$, $\Pi^\star \overset{\text{def}}{=} \Pi - \Pi^\#$ and $\Pi^\# \overset{\text{def}}{=} \overline{\sigma}^{-1}(f + \hat{v}_{\tilde{x}} - \hat{u}_{\tilde{y}})$ are the eddy Ertel PV flux, eddy and residual-mean Ertel PV respectively. Note $\Pi^\#$, computed from the residual-mean velocities, is different from the thickness-weighted Ertel PV, viz. $\hat{\Pi} = \frac{\overline{\Pi\sigma}}{\overline{\sigma}} = \overline{\sigma}^{-1}(f + \overline{v}_{\tilde{x}} - \overline{u}_{\tilde{y}})$. Equation (12) implies that if we are able to parametrize the eddy Ertel PV flux, equivalently we have parametrized the eddy feedback onto the mean flow encapsulated in the E-P flux divergence.

It is well known that the governing equation for Ertel PV is similar to that of passive tracers (S. K. Smith & Marshall, 2009; Vallis, 2017, Chapter 5), and that mesoscale eddies stir passive tracers along isopycnals (Redi, 1982; Gnanadesikan et al., 2015; Naveira Garabato et al., 2017; Griffies, 2018; Jones & Abernathey, 2019; Uchida et al., 2020). One significant difference between Ertel PV and passive tracers, however, is in its dynamical significance; the Ertel PV feeds back onto the dynamics in the form of eddy fluxes perhaps most well known in the transformed-Eulerian mean framework (e.g. Vallis, 2017, Chapter 10). This has led to the idea that the dynamical effect of mesoscale turbulence may be parametrized as a local gradient flux of the mean Ertel PV (Killworth, 1997; Great-

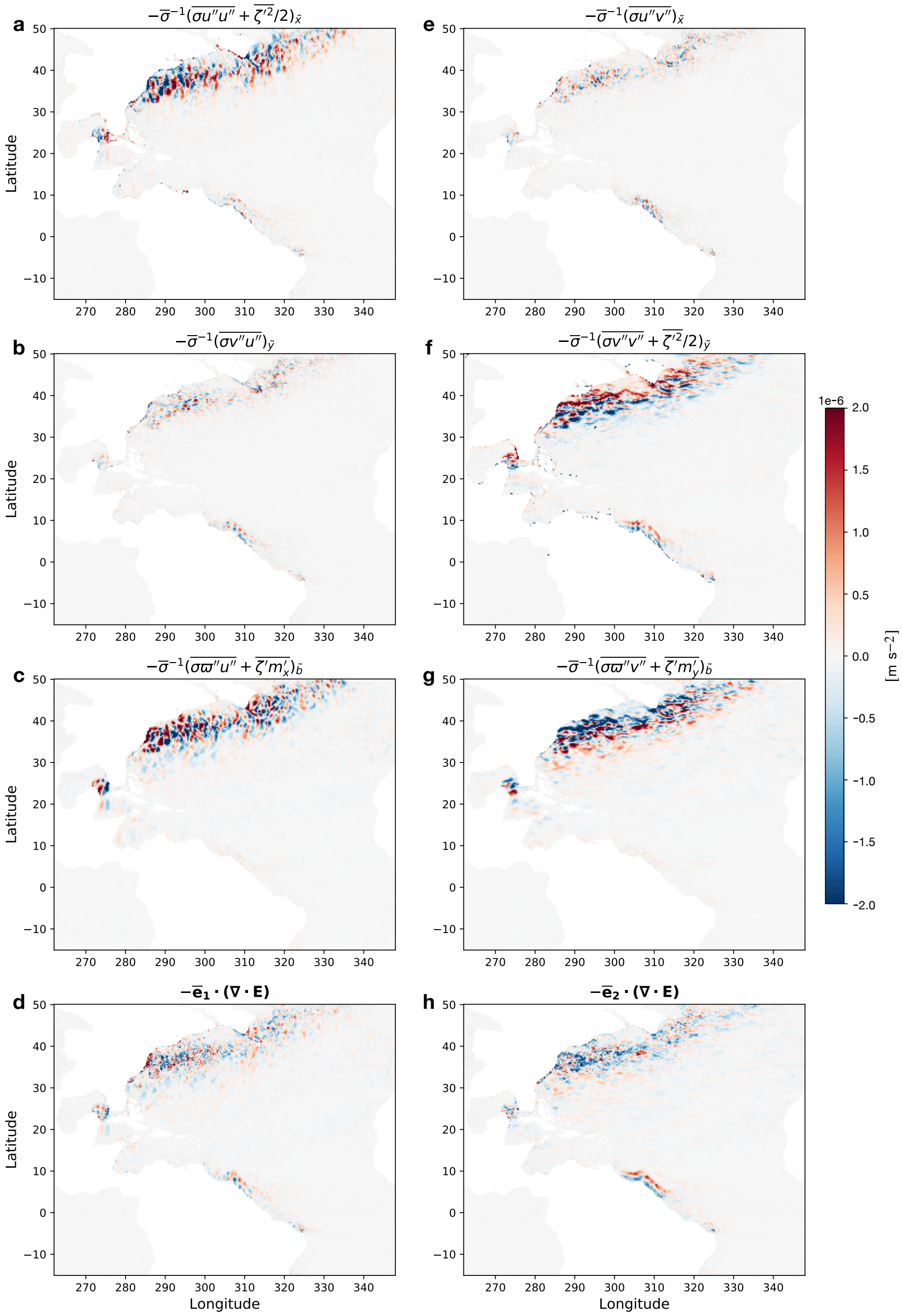

Figure 4. The terms in the divergence of E-P flux tensor on December 26, 1963 on the isopycnal layer as in Fig. 2. The red shadings indicate momentum being fluxed from the eddies to the mean flow and visa versa **a-c**,**e-g**. The panels are laid out so that summing up the top three rows per column yields the total zonal $(\overline{\mathbf{e}}_1 \cdot (\tilde{\nabla} \cdot \mathbf{E}))$ **d** and meridional E-P flux divergence $(\overline{\mathbf{e}}_2 \cdot (\tilde{\nabla} \cdot \mathbf{E}))$ **h** respectively.

batch, 1998; D. P. Marshall et al., 1999, 2012), i.e.

$$\widehat{\mathbf{u}''\Pi^\star} = -\kappa\tilde{\nabla}_{\mathrm{h}}\Pi^{\#} \ . \tag{13}$$

where κ is the eddy diffusivity. Equations (1), (2), (12) and (13) provide a pathway for a unique solution for the eddy closure problem as the E-P flux divergence is gauge invariant (J. R. Maddison & Marshall, 2013).

While it is tempting to directly infer a scalar eddy diffusivity from eqn. (13), assuming an isotropic diffusivity for an anisotropic flow as in our realistic simulation is a poor approximation (R. D. Smith & Gent, 2004; Ferrari & Nikurashin, 2010; Fox-Kemper et al., 2013). We, therefore, take the approach of estimating the eddy diffusivity tensor ($\mathbf{K}$) from a least-squares best fit to (Plumb & Mahlman, 1987; Abernathey et al., 2013; Bachman & Fox-Kemper, 2013):

$$\underbrace{\begin{pmatrix} \widehat{u''\theta''} & \widehat{v''\theta''} \\ \widehat{u''s''} & \widehat{v''s''} \\ \widehat{u''\Pi^\star} & \widehat{v''\Pi^\star} \end{pmatrix}}_{\mathbf{F}} = -\underbrace{\begin{pmatrix} \hat{\theta}_{\tilde{x}} & \hat{\theta}_{\tilde{y}} \\ \hat{s}_{\tilde{x}} & \hat{s}_{\tilde{y}} \\ \Pi^{\#}_{\tilde{x}} & \Pi^{\#}_{\tilde{y}} \end{pmatrix}}_{\mathbf{G}} \cdot \underbrace{\begin{pmatrix} \kappa^{uu} & \kappa^{vu} \\ \kappa^{uv} & \kappa^{vv} \end{pmatrix}}_{\mathbf{K}} . \tag{14}$$

In studies trying to parametrize the eddy-induced fluxes of isopycnal thickness in the buoyancy equation, they have always had the freedom to parametrize the flux itself or its divergence. This has caused some ambiguity regarding the whether the rotational component of eddy fluxes, often referred to as the gauge freedom, should be parametrized (discussed in depth by Griffies, 2018). However, since the TWA equations are forced directly by the eddy Ertel PV flux itself and not its divergence, we do not need to consider the discussion centred around rotational fluxes. In other words, eqn. (12) makes the case for parametrizing the *total* eddy flux, as opposed to solely its divergent component, when formulating a closure scheme for Ertel PV. The assumption that goes into eqn. (14) is that the eddy flux of temperature, salinity and Ertel PV behave statistically in a similar manner (Bachman et al., 2015). Since they are all active tracers, we would expect this assumption to hold to a good degree.

The least-squares fit can be estimated as $\mathbf{K} = \mathbf{G}^{+}\mathbf{F}$ where $\mathbf{G}^{+}$ is the Moore-Penrose psuedo inverse of $\mathbf{G}$ for each data point (Bachman et al., 2015). The gradients of the mean field, however, tended to be noisy due to errors accumulating from the remapping process (eqn. (4)). Therefore, we applied a convolutional spatial smoothing to the mean fields ($\hat{\theta}, \hat{s}, \Pi^{\#}$) prior to taking their gradient and eddy terms (viz. each element in $\mathbf{F}$) with a 5×5 Hann filter in the horizontal grid points using the `xscale` Python package (Sérazin, 2019). The spatial smoothing can be considered similar to a numerical convergence of the fields with an increase in the number of ensemble members. Each row in $\mathbf{F}$ and $\mathbf{G}$ was then normalized by horizontal median of the magnitude of each eddy fluxes (i.e. $\frac{(\widehat{\mathbf{u}''C''}, \mathbf{F}_C^{\mathrm{param}})}{\mathrm{median}[|\widehat{\mathbf{u}''C''}|]}$ where $\mathbf{F}_C^{\mathrm{param}}$ $(= \mathbf{G}_C \cdot \mathbf{K}_C)$ is the parametrized flux of an arbitrary tracer C) prior to the inversion so that each tracer had roughly equal weighting in inverting eqn. (14).

From Fig. 4, it is evident that the equatorial region contributes little to the Gulf Stream, so we will focus on north of 20N in this section. Figure 5a,d shows the diagnosed non-smoothed eddy Ertel PV flux, which we refer to as the "true" flux ($\mathbf{F}_\Pi^{\mathrm{true}}$), and its parametrized equivalent via eqn. (14) as a local-gradient flux of the mean Ertel PV (Fig. 5b,e). We see that the local-gradient flux closure successfully captures the spatial features of the true flux with the residual between the two being small (Fig. 5c,f). The residual comes from the smoothing we have applied prior to inverting eqn. (14) and/or errors in the remapping and discretization, but it is likely that this residual would decrease with an increase in the number of ensemble members. One may argue that since we are fitting the eddy diffusivities, the agreement is to be expected. It is nevertheless encouraging to see how well the eddy Ertel PV fluxes can be represented via an anisotropic eddy diffusivity tensor (Fig. 6) compared to previous studies reconstructing the eddy tracer fluxes with a scalar diffusivity (e.g. Wilson & Williams, 2006; J. Maddison et al., 2015). This also provides confidence to the assumption behind eqn. (14) that the Ertel PV behaves similarly to active tracers along isopycnals. In other words, along with the TWA framework, we have chosen the appropriate regression model to relate the total eddy transport of active tracers to their mean fields. Although it is possible to invert eqn. (14) with just two tracers, the inversion becomes ill defined unless their distributions are orthogonal to each other (Bachman et al., 2015). We have, therefore, kept it over-determined using three tracers.

The diffusivities presented in Fig. 6 are roughly on the same order as previous estimates based on satellite products (J. Marshall et al., 2006; Abernathey & Marshall, 2013; Klocker & Abernathey, 2014; Busecke et al., 2017; Bolton et al., 2019) and modelling studies (Wilson & Williams, 2006; Abernathey et al., 2013; Bachman & Fox-Kemper, 2013), which range spatially between $O(10^2$–$10^4)$ [m^2 s^{-1}]. The negative values, however, may come as a surprise. One of the key differences from the satellite-based estimates is that we do not assume an isotropic down-gradient flux closure with a scalar dif-

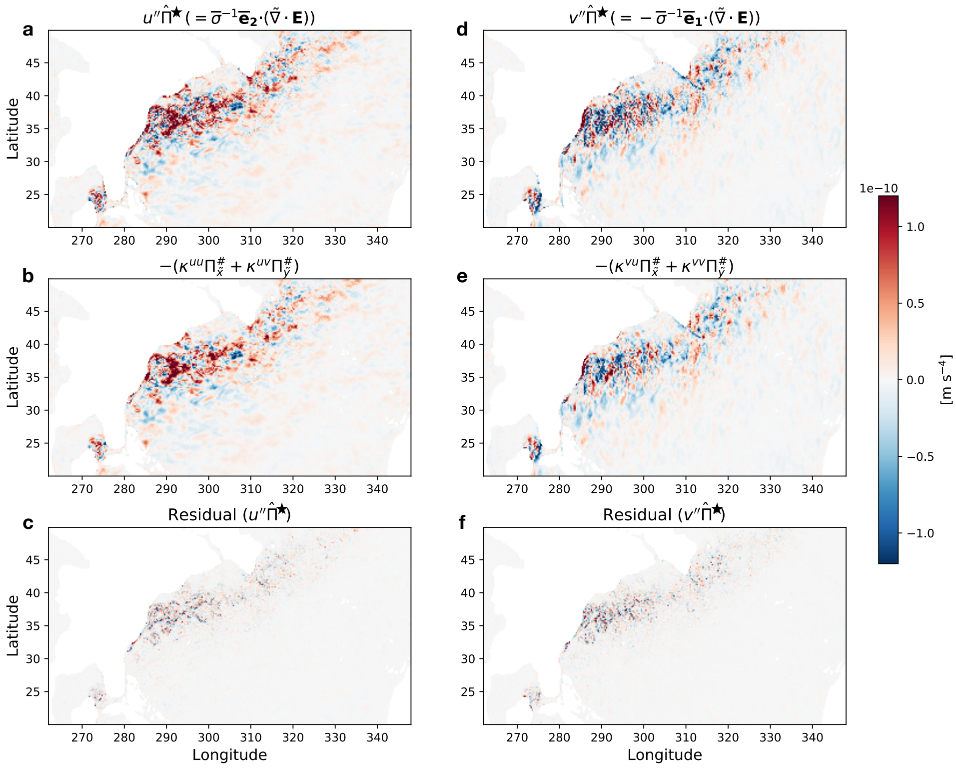

Figure 5. The diagnosed zonal and meridional eddy PV flux on December 26, 1963 on the isopycnal layer as in Fig. 2. We see a strong signal in the Gulf Stream region **a**,**d**. **b**,**e** The parametrized eddy PV flux via eqn. (14). **c**,**f** The residual between the true and parametrized eddy PV flux.

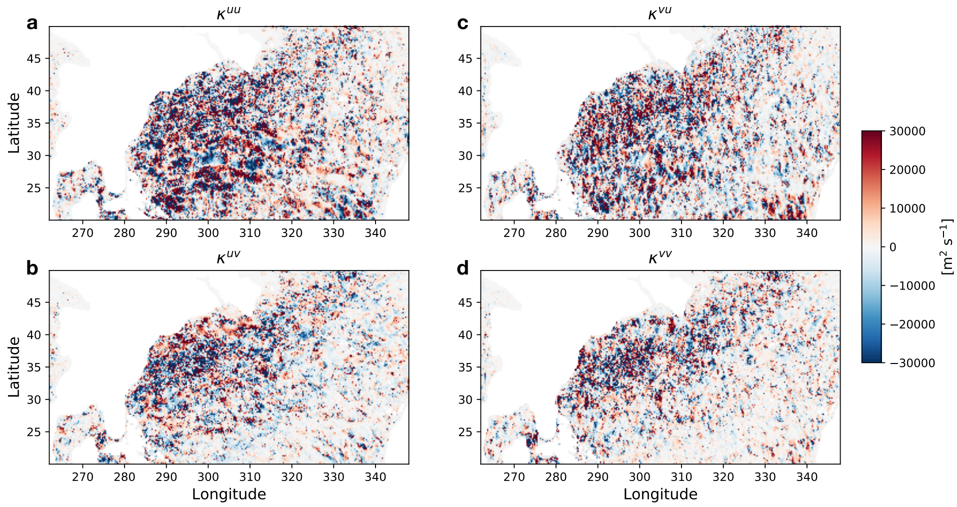

Figure 6. The diagnosed eddy diffusivity parameters via eqn. (14) in the diffusivity tensor **K** on December 26, 1963 on the isopycnal layer as in Fig. 2.

fusivity. In other words, the negative "κ"s do not necessarily translate to up-gradient tracer fluxes as, based on eqn. (14), the closure is a linear combination of the zonal and meridional gradients; the fluxes could be down gradient in the two-dimensional sense. On the other hand, in cases where the eddy fluxes are locally oriented up gradient of the mean tracer field, negative "κ"s would be a faithful representation of this. We show the inner angle between the eddy flux and gradient of the mean field:

$$\varphi_C = \arccos\left[\frac{\mathbf{F}_C^{\text{true}} \cdot \mathbf{G}_C}{|\mathbf{F}_C^{\text{true}}||\mathbf{G}_C|}\right] \tag{15}$$

in Fig. 7 for each tracer; a down-gradient eddy flux would result in $\varphi \sim 0$. There are regions of both down-gradient and up-gradient eddy fluxes for all three tracers (Fig. 7). Although the eddy fluxes should be down gradient of the mean field in the global sense in order to allow for the homogenization of tracers (D. P. Marshall et al., 2012; J. R. Maddison & Marshall, 2013), a locally up-gradient eddy flux is associated with an up-gradient transfer of tracer variance. It should not be surprising that in a realistic simulation, instantaneous fields of tracer variance can be spatially inhomogenous with sources, sinks and transport of variance (Wilson & Williams, 2006). In the context of energy-backscattering eddy parametrizations, when the tracer is Ertel PV, an up-gradient eddy flux is equivalent to the eddies fluxing momentum back into the mean flow, which is precisely the effect we would want to represent.

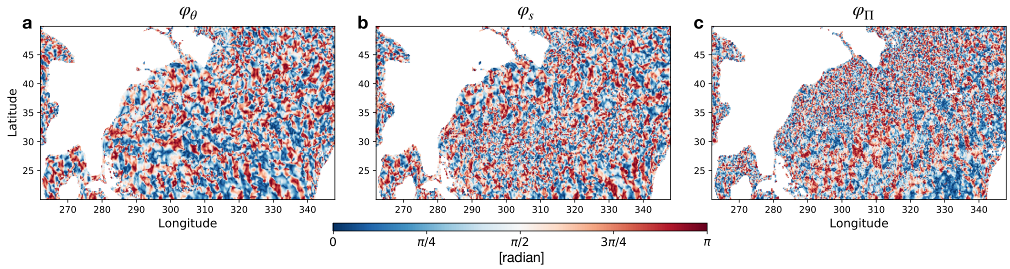

Figure 7. The inner angle between the eddy flux and horizontal gradient of the mean on December 26, 1963 for potential temperature (φ_θ) **a**, practical salinity (φ_s) **b** and Ertel PV (φ_Π) **c** on the isopycnal layer as in Fig. 2. The angles are close to zero when the eddy flux is oriented down gradient of the mean Ertel PV and close to π when oriented up gradient.

It is also informative to examine the diffusive component of the diffusivity tensor in regards to isopycnic tracer mixing, i.e. the eigenvalues of the symmetric part of the tensor ($\mathbf{S} \overset{\text{def}}{=} \frac{1}{2}(\mathbf{K}+\mathbf{K}^{\mathrm{T}})$ where $\mathbf{K}^{\mathrm{T}}$ is the transpose). The spatial median of the eigenvalues along the major-axis (λ^M) and minor-axis (λ^m) of eigenvectors on December 26, 1963 (Fig. 6) are 1286 (12119) m^2 s^{-1} and 56 (2247) m^2 s^{-1} respectively with a long tail in both positive and negative values. The values in curly brackets show the median of the normed diffusivities $|\lambda^M|$ and $|\lambda^m|$ respectively. The negative values likely come from the mean flow being strongly inhomogeneous. The spatial median of the anisotropy parameter ($|\lambda^M|/|\lambda^m|$) is around 4.6. Although the order of magnitude of the eigenvalues is similar to previous modelling studies (e.g. Abernathey et al., 2013), it is difficult to make a direct comparison due to the differences in the averaging operator and model configuration.

We end this section by showing the spatial correlation and error between the true and parametrized eddy flux along the temporal and buoyancy dimensions:

$$r_C = \frac{\sum[(F_C^{\text{true}} - \langle F_C^{\text{true}}\rangle)(F_C^{\text{param}} - \langle F_C^{\text{param}}\rangle)]}{\sqrt{\sum(F_C^{\text{true}} - \langle F_C^{\text{true}}\rangle)^2}\sqrt{\sum(F_C^{\text{param}} - \langle F_C^{\text{param}}\rangle)^2}} \ , \tag{16}$$

$$\mathcal{E}_C \overset{\text{def}}{=} \frac{|F_C^{\text{true}} - F_C^{\text{param}}|}{|F_C^{\text{true}}|} \tag{17}$$

where $\langle\cdot\rangle$ is the horizontal domain average. Equations (16) and (17) were calculated using every three grid points in the zonal and meridional dimension between 20N-50N, and every two grid points in the buoyancy dimension across the range roughly corresponding to depths between 300–2000 m. The correlation is generally higher than 0.9 for potential temperature and 0.5 for practical salinity across all seasons in the quasi-adiabatic

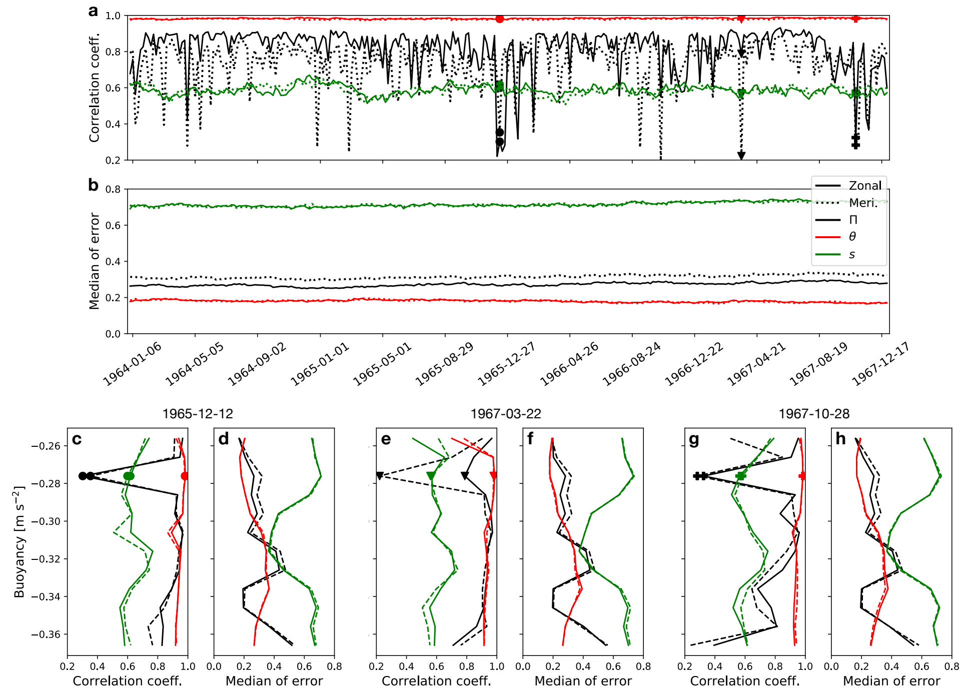

Figure 8. The correlation coefficient and spatial median of the error for potential temperature (red; $r_\theta, \mathcal{E}_\theta$), practical salinity (green; $r_s, \mathcal{E}_s$) and Ertel PV (black; $r_\Pi, \mathcal{E}_\Pi$). The zonal component is shown in solid lines and the meridional in dotted lines. **a**,**b** The correlation coefficients and error on the isopycnal as in Fig. 2. The circle, triangle and plus markers indicate the dates we show the vertical profiles. **c-h** The vertical profiles on December 12, 1965, March 22, 1967 and October 28, 1967.

interior for the latter four years of output we have (Fig. 8). The performance of Ertel PV is between the two ($r_\Pi \sim 0.8$) with large temporal fluctuations. The spatial correlation is sensitive to extrema due to its dependence on the spatial mean ($\langle F_\Pi \rangle$; eqn. (16)), likely responsible for the fluctuations as the spatial median of the error is stable over the entire time series ($\mathcal{E}_\Pi \sim 0.3$; Fig. 8b). The robustness of our parametrization can also be seen from the vertical structure of the error (Fig. 8d,f,h); it shows very little temporal variation regardless of the date.

5 Discussion and summary

By running a 12-member ensemble run of the North Atlantic Ocean at mesoscale resolving resolution (1/12°), we have shown that the thickness-weighted average (TWA) framework can be employed successfully in diagnosing eddy-mean flow interactions in a realistic ocean simulation. The ensemble approach negates the necessity for any temporal averaging in defining the residual-mean flow; we are able to exclude any temporal variability, such as seasonal and interannual fluctuations, from the eddy term and extract the intrinsic mesoscale variability of the ocean. We show that the Eliassen-Palm (E-P) flux divergence, which encapsulates the eddy feedback onto the mean flow (J. R. Maddison & Marshall, 2013), tends to meridionally decelerate the Gulf Stream (Fig. 4h). Modelling studies with varying spatial resolution have shown that the Gulf Stream tends to overshoot northwards in coarse resolution models (e.g. Lévy et al., 2010; Chassignet & Xu, 2017). The meridional deceleration implies that this overshooting may partially be attributable to mesoscale eddy feedback, in particular baroclinic instability (Fig. 4g), being insufficiently resolved at such resolutions, in addition to submesoscale boundary layer processes (e.g. Renault et al., 2016; Schoonover et al., 2017). The overshooting is also apparent in our simulation (Fig. 2d) implying that even models with the resolution of $1/12^\circ$ could benefit from parametrizing the eddy momentum fluxes.

In the TWA framework, the eddy Ertel potential vorticity (Ertel PV) flux is directly related to the E-P flux divergence (Young, 2012). In the context of eddy parametrization, this implies that if we can parametrize the eddy Ertel PV flux, we have a solution for the mesoscale eddy closure problem, which we provide in Figs. 5 and 6. We would like to emphasize that the eddy diffusivities presented in this paper are diagnostic rather than prognostic variables. Future work would need to examine how each parameter in the eddy diffusivity tensor ($\mathbf{K}$; eqn. (14)) is determined by the residual-mean field for a prognostic eddy closure scheme. Data-driven methods may be a viable way to discover such equations to constrain the "κ"s (e.g. Zhang & Lin, 2018; Zanna & Bolton, 2020). While it is beyond the scope of this study, it would also be interesting to examine the relation between the "κ"s and eddy shape, orientation and/or energy (e.g. D. P. Marshall et al., 2012; Waterman & Lilly, 2015; Bachman et al., 2017; Anstey & Zanna, 2017; Mak et al., 2018; Poulsen et al., 2019).

Nevertheless, we have shown that the eddy Ertel PV flux can be parametrized as an active tracer by a local-gradient flux closure across all seasons (Fig. 8). The apparent success of our diffusivity tensor lies on the fact that it relates the eddy fluxes to the residual-mean as opposed to the Eulerian-mean fields. As was noted by McDougall and McIntosh (2001) and Young (2012), the TWA framework allows one to shift the focus of eddy parametrization from the buoyancy equation to the momentum equations (1) and (2). What follows is that the tensor **K** includes information of not only the (eddy-induced) skew-diffusive flux of isopycnal thickness (Gent & Mcwilliams, 1990; Griffies, 1998) and isopycnic tracer diffusivity (Redi, 1982), but also the eddy momentum fluxes, which energy backscattering eddy parametrizations are being developed to represent (e.g. Kitsios et al., 2013; Bachman et al., 2018; Bachman, 2019; Zanna & Bolton, 2020; Jansen et al., 2019; Perezhogin, 2019; Juricke et al., 2020). Although there are four parameters in the tensor **K**, this is no more than assuming, for example, spatial variability and anisotropy in the isopycnal skew diffusivity (Gent & Mcwilliams, 1990; Griffies, 1998) and isopycnic tracer diffusivity (Redi, 1982). We believe our results provide a robust framework to evaluate such newly developed parametrizations in primitive equation models, i.e. they should be representing the E-P flux divergence, and a first step towards a unified mesoscale eddy closure scheme.

Appendix A Neutral surfaces as the coordinate system

Suppose we use neutrally-surfaced density (Stanley, 2019) to define the coordinate system, i.e. $\tilde{b} = -g\delta\rho/\rho_0$, which we will refer to as neutral buoyancy, where $\delta\rho$ is the neutrally-surfaced density anomaly. The Montgomery potential then becomes $m(\tilde{b}) = \phi(\tilde{b}) - b(\tilde{b})\zeta(\tilde{b})$ where b is the in-situ buoyancy defined by in-situ density and satisfies $\phi_{\tilde{\zeta}} = b$. Hence, the hydrostatic balance (eqn. (109) in Young, 2012) becomes:

$$\begin{aligned} m_{\tilde{b}} &= (\phi - b\zeta)_{\tilde{b}} \\ &= \phi_{\tilde{b}} - b_{\tilde{b}}\zeta - b\zeta_{\tilde{b}} \\ &= -b_{\tilde{b}}\zeta. \end{aligned}$$

Although it is possible to continue on by carrying around the Jacobian term keeping in mind that $b_{\tilde{b}} \neq 1$, the simplicity of the TWA framework is lost down the line due to the chain rule. An example being:

$$\begin{aligned} \tilde{\nabla}_{\mathrm{h}} m &= \nabla_{\mathrm{h}} m - m_{\tilde{b}} \nabla_{\mathrm{h}} b && \text{(A1)} \\ &= \nabla_{\mathrm{h}} m + b_{\tilde{b}}\zeta \nabla_{\mathrm{h}} b && \text{(A2)} \\ &= \nabla_{\mathrm{h}}(\phi - b\zeta) + b_{\tilde{b}}\zeta \nabla_{\mathrm{h}} b && \text{(A3)} \end{aligned}$$

where the right-hand side of (A3) is not equivalent to $\nabla_{\mathrm{h}}\phi$.

Appendix B Energetics under a non-linear equation of state

The TWA residual-mean horizontal momentum equation in geopotential coordinates neglecting dissipation is (Young, 2012):

$$\hat{\mathbf{u}}_{\tilde{t}} + \mathbf{v}^{\#} \cdot \nabla \hat{\mathbf{u}} + \mathbf{f} \times \hat{\mathbf{u}} = -\nabla_{\mathrm{h}} \phi^{\#} - \nabla_{\mathrm{h}} \cdot \mathbf{E}, \tag{B1}$$

where $\mathbf{v}^{\#} \stackrel{\mathrm{def}}{=} (\hat{\mathbf{u}}, w^{\#})$ so the residual-mean kinetic energy ($K^{\#} = |\hat{\mathbf{u}}|^2/2$) budget becomes:

$$K^{\#}_t + \mathbf{v}^{\#} \cdot \nabla K^{\#} = -\hat{\mathbf{u}} \cdot \nabla_{\mathrm{h}} \phi^{\#} - \hat{\mathbf{u}} \cdot (\nabla_{\mathrm{h}} \cdot \mathbf{E}) \tag{B2}$$

$$= -\hat{\mathbf{u}} \cdot \nabla_{\mathrm{h}} \phi^{\#} - w^{\#} \phi^{\#}_z + w^{\#} b^{\#} - \hat{\mathbf{u}} \cdot (\nabla_{\mathrm{h}} \cdot \mathbf{E}) \tag{B3}$$

$$= -\mathbf{v}^{\#} \cdot \nabla \phi^{\#} + w^{\#} b^{\#} - \hat{\mathbf{u}} \cdot (\nabla_{\mathrm{h}} \cdot \mathbf{E}). \tag{B4}$$

We can now define the mean potential enthalpy as (McDougall, 2003):

$$h^{\#} \stackrel{\mathrm{def}}{=} \int_{\Phi_0}^{\Phi} \frac{b^{\#}}{\rho_0 g} d\Phi^{\#} \tag{B5}$$

where $\Phi^{\#} = \Phi_0 - \rho_0 g z$ is the dynamically non-active part of the hydrostatic pressure to be consistent with the Boussinesq approximation. It is important to keep in mind that the "z" here is the average depth of an isopycnal surface (i.e. $z = \overline{\zeta}(\tilde{t}, \tilde{x}, \tilde{y}, b^{\#})$). The mean advective derivative of $h^{\#}$ is:

$$\mathbf{v}^{\#} \cdot \nabla h^{\#} = h^{\#}_{\Phi^{\#}} \mathbf{v}^{\#} \cdot \nabla \Phi^{\#} + h^{\#}_{\hat{\theta}} \mathbf{v}^{\#} \cdot \nabla \hat{\theta} + h^{\#}_{\hat{s}} \mathbf{v}^{\#} \cdot \nabla \hat{s} \tag{B6}$$

$$= -w^{\#} b^{\#} + h^{\#}_{\hat{\theta}} \mathbf{v}^{\#} \cdot \nabla \hat{\theta} + h^{\#}_{\hat{s}} \mathbf{v}^{\#} \cdot \nabla \hat{s} \tag{B7}$$

Therefore,

$$K^{\#}_t + \mathbf{v}^{\#} \cdot \nabla (K^{\#} + h^{\#}) = -\mathbf{v}^{\#} \cdot \nabla \phi^{\#} + J^{\#}_h - \hat{\mathbf{u}} \cdot (\nabla_{\mathrm{h}} \cdot \mathbf{E}) \tag{B8}$$

where $J^{\#}_h \stackrel{\mathrm{def}}{=} h^{\#}_{\hat{\theta}} \mathbf{v}^{\#} \cdot \nabla \hat{\theta} + h^{\#}_{\hat{s}} \mathbf{v}^{\#} \cdot \nabla \hat{s}$.

On the other hand, the TWA budget of total kinetic energy is:

$$\frac{1}{2}(\widehat{|\mathbf{u}|^2}_{\tilde{t}} + \tilde{\nabla} \cdot \widehat{\mathbf{v}|\mathbf{u}|^2}) = -\tilde{\nabla} \cdot \widehat{\mathbf{v}\phi} + \hat{w}\tilde{b} \tag{B9}$$

$$= -\tilde{\nabla} \cdot \widehat{\mathbf{v}\phi} - \tilde{\nabla} \cdot \widehat{\mathbf{v}h} + h_\theta \widehat{\nabla \cdot (\mathbf{v}\theta)} + h_s \widehat{\nabla \cdot (\mathbf{v}s)}, \tag{B10}$$

where $\tilde{\nabla} \cdot$ is the three-dimensional divergence in buoyancy coordinates, and using the relation $\overline{\sigma\phi\theta} = \overline{\sigma}(\hat{\phi}\hat{\theta} + \widehat{\phi''\theta''})$ (eqn. (72) in Young, 2012) yields:

$$\frac{1}{2}\left[\widehat{|\mathbf{u}|^2}_{\tilde{t}} + \tilde{\nabla} \cdot (\hat{\mathbf{v}}\widehat{|\mathbf{u}|^2} + \widehat{\mathbf{v}''|\mathbf{u}|^{2\prime\prime}})\right] = -\tilde{\nabla} \cdot \widehat{\mathbf{v}\phi} - \tilde{\nabla} \cdot (\hat{\mathbf{v}}\hat{h} + \widehat{\mathbf{v}''h''}) + \hat{J}_h, \tag{B11}$$

where $\hat{\mathbf{v}} \overset{\text{def}}{=} \hat{u}\overline{\mathbf{e}}_1 + \hat{v}\overline{\mathbf{e}}_2 + \overline{\sigma}^{-1}(\overline{\zeta}_{\tilde{t}} + \hat{\varpi}\overline{\zeta}_{\tilde{b}})\overline{\mathbf{e}}_3$ and $\hat{J}_h \overset{\text{def}}{=} h_\theta \widehat{\nabla \cdot (\mathbf{v}\theta)} + h_s \widehat{\nabla \cdot (\mathbf{v}s)}$. Now, realizing that $\widehat{|\mathbf{u}|^2} = |\hat{\mathbf{u}}|^2 + \widehat{|\mathbf{u}''|^2} \overset{\text{def}}{=} 2(K^\# + K'')$, we get:

$$K^\#_{\tilde{t}} + K''_{\tilde{t}} + \tilde{\nabla} \cdot \left[\hat{\mathbf{v}}(K^\# + K'' + \hat{h}) + \widehat{\mathbf{v}''|\mathbf{u}|^{2''}} + \widehat{\mathbf{v}''h''}\right] = -\tilde{\nabla} \cdot \widehat{\mathbf{v}\phi} + \hat{J}_h, \tag{B12}$$

which can be rewritten using the coordinate-invariant differential operator as:

$$K^\#_t + K''_t + \nabla \cdot [\mathbf{v}^\#(K^\# + K'' + \hat{h})] + \nabla \cdot (\widehat{\mathbf{v}''|\mathbf{u}|^{2''}} + \widehat{\mathbf{v}''h''}) = -\nabla \cdot \widehat{\mathbf{v}\phi} + \hat{J}_h. \tag{B13}$$

Hence, subtracting eqn. (B8) from (B13) yields:

$$K''_t + \nabla \cdot \left[\mathbf{v}^\#(K'' + \hat{h} - h^\#)\right] = -\nabla \cdot \left[\widehat{\mathbf{v}''|\mathbf{u}|^{2''}} + \widehat{\mathbf{v}''h''} + \widehat{\mathbf{v}\phi} - \mathbf{v}^\#\phi^\#\right] + \hat{J}_h - J^\#_h + \hat{\mathbf{u}} \cdot (\nabla_{\mathrm{h}} \cdot \mathbf{E}). \tag{B14}$$

Equations (B8) and (B14) are the relations derived by Aoki (2014) but for a non-linear equation of state (EOS) where the residual-mean flow and eddies exchange energy via the E-P flux divergence.

For a linear EOS, the eddy potential energy (EPE; $\hat{h} - h^\#$) in eqn. (B14) can be rewritten as:

$$\hat{h} - h^\# = -b^\#(\hat{\zeta} - \overline{\zeta}) \tag{B15}$$

$$= -b^\# \frac{\overline{\sigma'\zeta'}}{\overline{\sigma}} \tag{B16}$$

by taking advantage of $\hat{h} = -\tilde{b}\hat{\zeta}$, $h^\# = -b^\#\overline{\zeta}$ and $\tilde{b} = b^\#(t, x, y, \overline{\zeta})$. Equation (B15) provides the physical intuition of EPE being defined as the difference between potential energy defined at the thickness-weighted and ensemble-averaged isopycnal depths.

Appendix C Kinematics of discretization

As in Fig. C1, imagine u_1 and u_2 are on the same buoyancy contour. The relation between the two is:

$$u_2 = u_1 + u_x \Delta x + u_\zeta \Delta\zeta. \tag{C1}$$

$$\therefore \ u_{\tilde{x}} \overset{\text{def}}{=} u_x + u_\zeta \frac{\Delta\zeta}{\Delta x} = \frac{u_2 - u_1}{\Delta x} \tag{C2}$$

so once all of the variables are remapped onto the buoyancy coordinate from geopotential, the discretized horizontal gradients can be taken along the original Cartesian grid. The gradients on the model outputs were taken using the `xgcm` Python package (Abernathey & Busecke, 2019; Busecke & Abernathey, 2020). In order to minimize the discretization error, we take the ensemble mean first whenever possible, e.g. $\overline{\sigma} = \overline{\partial_{\tilde{b}}\zeta} = \partial_{\tilde{b}}\overline{\zeta}$, $\tilde{\nabla}_{\mathrm{h}}\overline{\sigma} =$

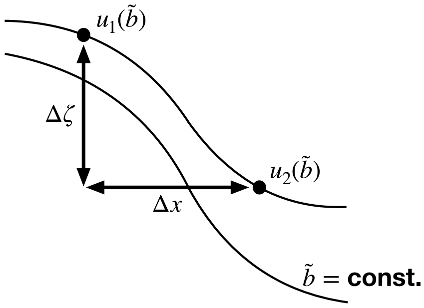

Figure C1. Schematic of discretized gradients.

$\partial_{\tilde{b}}\tilde{\nabla}_{\mathrm{h}}\overline{\zeta}$ etc. The gradient operators commuting with the ensemble mean is also the case for the perturbations, i.e.

$$\tilde{\nabla}_{\mathrm{h}}(\overline{m} + m') = \tilde{\nabla}_{\mathrm{h}}m = \overline{\tilde{\nabla}_{\mathrm{h}}m} + (\tilde{\nabla}_{\mathrm{h}}m)'. \tag{C3}$$

Hence, $\tilde{\nabla}_{\mathrm{h}}m' = (\tilde{\nabla}_{\mathrm{h}}m)'$ (c.f. J. R. Maddison & Marshall, 2013, Section 2.3 in their paper).

Acknowledgments

This research was funded by the French 'Make Our Planet Great Again' (MOPGA) initiative managed by the Agence Nationale de la Recherche under the Programme d'Investissement d'Avenir, with the reference ANR-18-MPGA-0002. High-performance computing resources on Cheyenne (doi:10.5065/D6RX99HX) used for running the ensembles were provided by NCAR's Computational and Information Systems Laboratory, sponsored by the National Science Foundation, under the university large allocation UFSU0011. The simulation outputs are available on the Florida State University cluster (`http://ocean.fsu.edu/~qjamet/share/data/twa_Uchida/`). Python scripts used for the off-line diagnosis are available on Github (`doi:10.5281/zenodo.4002824`). Uchida acknowledges Spencer Jones for developing the `xlayers` Python package (`doi:10.5281/zenodo.3659227`), Ryan Abernathey and Julius Busecke for the `xgcm` Python package (`doi:10.5281/zenodo.3634752`), and Guillaume Sérazin for the `xscale` Python package for parallelized convolutional spatial filtering (`doi:10.5281/zenodo.322362`).

References

Abernathey, R. P. (2020). `fastjmd95`*: Numba implementation of jackett & mcdougall (1995) ocean equation of state.* Retrieved from `https://github.com/`

`xgcm/fastjmd95`

Abernathey, R. P., & Busecke, J. (2019). `xgcm`*: General circulation model post-processing with xarray.* Retrieved from `https://xgcm.readthedocs.io/en/latest/` doi: 10.5281/zenodo.3634752

Abernathey, R. P., Ferreira, D., & Klocker, A. (2013). Diagnostics of isopycnal mixing in a circumpolar channel. *Ocean Modelling*, *72*, 1–16.

Abernathey, R. P., & Marshall, J. (2013). Global surface eddy diffusivities derived from satellite altimetry. *Journal of Geophysical Research: Oceans*, *118*(2), 901–916.

Aiki, H., & Richards, K. J. (2008). Energetics of the global ocean: the role of layer-thickness form drag. *Journal of physical oceanography*, *38*(9), 1845–1869.

Ajayi, A., Le Sommer, J., Chassignet, E., Molines, J.-M., Xu, X., Albert, A., & Cosme, E. (2020). Spatial and temporal variability of the north atlantic eddy field from two kilometric-resolution ocean models. *Journal of Geophysical Research: Oceans*. doi: 10.1029/2019JC015827

Aluie, H., Hecht, M., & Vallis, G. K. (2018). Mapping the energy cascade in the north atlantic ocean: The coarse-graining approach. *Journal of Physical Oceanography*, *48*(2), 225–244.

Anstey, J. A., & Zanna, L. (2017). A deformation-based parametrization of ocean mesoscale eddy reynolds stresses. *Ocean Modelling*, *112*, 99–111.

Aoki, K. (2014). A constraint on the thickness-weighted average equation of motion deduced from energetics. *Journal of Marine Research*, *72*(5), 355–382.

Aoki, K., Kubokawa, A., Furue, R., & Sasaki, H. (2016). Influence of eddy momentum fluxes on the mean flow of the kuroshio extension in a 1/10 ocean general circulation model. *Journal of Physical Oceanography*, *46*(9), 2769–2784.

Arbic, B. K., Polzin, K. L., Scott, R. B., Richman, J. G., & Shriver, J. F. (2013). On eddy viscosity, energy cascades, and the horizontal resolution of gridded satellite altimeter products. *Journal of Physical Oceanography*, *43*(2), 283–300.

Bachman, S. D. (2019). The gm+ e closure: A framework for coupling backscatter with the gent and mcwilliams parameterization. *Ocean Modelling*, *136*, 85–106.

Bachman, S. D., Anstey, J. A., & Zanna, L. (2018). The relationship between a deformation-based eddy parameterization and the lans-α turbulence model. *Ocean Modelling*, *126*, 56–62.

Bachman, S. D., & Fox-Kemper, B. (2013). Eddy parameterization challenge suite i: Eady spindown. *Ocean Modelling*, *64*, 12–28.

Bachman, S. D., Fox-Kemper, B., & Bryan, F. O. (2015). A tracer-based inversion method for diagnosing eddy-induced diffusivity and advection. *Ocean Modelling*, *86*, 1–14.

Bachman, S. D., Marshall, D. P., Maddison, J. R., & Mak, J. (2017). Evaluation of a scalar eddy transport coefficient based on geometric constraints. *Ocean Modelling*, *109*, 44–54.

Balwada, D., Smith, S. K., & Abernathey, R. P. (2018). Submesoscale vertical velocities enhance tracer subduction in an idealized antarctic circumpolar current. *Geophysical Research Letters*, *45*(18), 9790–9802.

Bire, S., & Wolfe, C. L. (2018). The role of eddies in buoyancy-driven eastern boundary currents. *Journal of Physical Oceanography*, *48*(12), 2829–2850.

Bolton, T., Abernathey, R. P., & Zanna, L. (2019). Regional and temporal variability of lateral mixing in the north atlantic. *Journal of Physical Oceanography*, *49*(10), 2601–2614.

Busecke, J., & Abernathey, R. P. (2020). Cmip6 without the interpolation: Grid-native analysis with pangeo in the cloud. In *2020 earthcube annual meeting.* Retrieved from `https://github.com/earthcube2020/ec20_busecke_etal`

Busecke, J., Abernathey, R. P., & Gordon, A. L. (2017). Lateral eddy mixing in the subtropical salinity maxima of the global ocean. *Journal of Physical Oceanography*, *47*(4), 737–754.

Capet, X., McWilliams, J. C., Molemaker, M. J., & Shchepetkin, A. (2008). Mesoscale to submesoscale transition in the california current system. part iii: Energy balance and flux. *Journal of Physical Oceanography*, *38*(10), 2256–2269.

Cessi, P., & Wolfe, C. L. (2013). Adiabatic eastern boundary currents. *Journal of Physical Oceanography*, *43*(6), 1127–1149.

Chassignet, E. P., & Xu, X. (2017). Impact of horizontal resolution (1/12° to 1/50°) on gulf stream separation, penetration, and variability. *Journal of Physical Oceanography*, *47*(8), 1999–2021.

de Boyer Montégut, C., Madec, G., Fischer, A. S., Lazar, A., & Iudicone, D. (2004). Mixed layer depth over the global ocean: An examination of profile data and a profile-based climatology. *Journal of Geophysical Research: Oceans*, *109*(C12).

Deremble, B., Wienders, N., & Dewar, W. (2013). Cheapaml: A simple, atmospheric boundary layer model for use in ocean-only model calculations. *Monthly weather review*, *141*(2), 809–821.

De Szoeke, R. A., & Bennett, A. F. (1993). Microstructure fluxes across density surfaces. *Journal of physical oceanography*, *23*(10), 2254–2264.

Fairall, C. W., Bradley, E. F., Hare, J. E., Grachev, A. A., & Edson, J. B. (2003). Bulk parameterization of air–sea fluxes: Updates and verification for the coare algorithm. *Journal of climate*, *16*(4), 571–591.

Ferrari, R., & Nikurashin, M. (2010). Suppression of eddy diffusivity across jets in the southern ocean. *Journal of Physical Oceanography*, *40*(7), 1501–1519.

Fox-Kemper, B., Lumpkin, R., & Bryan, F. O. (2013). Lateral transport in the ocean interior. In *International geophysics* (Vol. 103, pp. 185–209). Elsevier.

Gent, P. R., & Mcwilliams, J. C. (1990). Isopycnal mixing in ocean circulation models. *Journal of Physical Oceanography*, *20*(1), 150–155.

Gnanadesikan, A., Pradal, M.-A., & Abernathey, R. P. (2015). Isopycnal mixing by mesoscale eddies significantly impacts oceanic anthropogenic carbon uptake. *Geophysical Research Letters*, *42*(11), 4249–4255.

Greatbatch, R. J. (1998). Exploring the relationship between eddy-induced transport velocity, vertical momentum transfer, and the isopycnal flux of potential vorticity. *Journal of Physical Oceanography*, *28*(3), 422–432.

Griffies, S. M. (1998). The gent–mcwilliams skew flux. *Journal of Physical Oceanography*, *28*(5), 831–841.

Griffies, S. M. (2018). *Fundamentals of ocean climate models.* Princeton university press.

Griffies, S. M., Winton, M., Anderson, W. G., Benson, R., Delworth, T. L., Dufour, C. O., … others (2015). Impacts on ocean heat from transient mesoscale eddies in a hierarchy of climate models. *Journal of Climate*, *28*(3), 952–977.

Hawkins, E., Smith, R. S., Gregory, J. M., & Stainforth, D. A. (2016). Irreducible uncertainty in near-term climate projections. , *46*(11-12), 3807–3819.

Jackett, D. R., & Mcdougall, T. J. (1995). Minimal adjustment of hydrographic profiles to achieve static stability. *Journal of Atmospheric and Oceanic Technology*, *12*(2), 381–389.

Jamet, Q., Dewar, W., Wienders, N., & Deremble, B. (2019a). Fast warming of the surface ocean under a climatological scenario. *Geophysical Research Letters*, *46*(7), 3871–3879.

Jamet, Q., Dewar, W. K., Wienders, N., & Deremble, B. (2019b). Spatiotemporal patterns of chaos in the atlantic overturning circulation. *Geophysical Research Letters*, *46*(13), 7509–7517.

Jamet, Q., Dewar, W. K., Wienders, N., Deremble, B., Close, S., & Penduff, T. (2020). Locally and remotely forced subtropical amoc variability: A matter of time scales. *Journal of Climate*. doi: 10.1175/JCLI-D-19-0844.1

Jansen, M. F., Adcroft, A., Khani, S., & Kong, H. (2019). Toward an energetically consistent, resolution aware parameterization of ocean mesoscale eddies. *Journal of Advances in Modeling Earth Systems*, *11*(8), 2844–2860.

Jones, S. C. (2019). `xlayers`*: Python implementation of mitgcm's layer package.* Retrieved from `https://github.com/cspencerjones/xlayer` doi: 10.5281/zenodo.3659227

Jones, S. C., & Abernathey, R. P. (2019). Isopycnal mixing controls deep ocean ventilation. *Geophysical Research Letters*. doi: 10.1029/2019GL085208

Jones, S. C., Busecke, J., Uchida, T., & Abernathey, R. P. (2020). Vertical regridding and remapping of cmip6 ocean data in the cloud. In *2020 earthcube annual meeting.* Retrieved from `https://github.com/earthcube2020/ec20_jones_etal`

Juricke, S., Danilov, S., Koldunov, N., Oliver, M., & Sidorenko, D. (2020). Ocean kinetic energy backscatter parametrization on unstructured grids: Impact on global eddy-permitting simulations. *Journal of Advances in Modeling Earth Systems*, *12*(1).

Killworth, P. D. (1997). On the parameterization of eddy transfer part i. theory. *Journal of Marine Research*, *55*(6), 1171–1197.

Kitsios, V., Frederiksen, J. S., & Zidikheri, M. J. (2013). Scaling laws for parameterisations of subgrid eddy–eddy interactions in simulations of oceanic circulations. *Ocean Modelling*, *68*, 88–105.

Kjellsson, J., & Zanna, L. (2017). The impact of horizontal resolution on energy transfers in global ocean models. *Fluids*, *2*(3), 45.

Klocker, A., & Abernathey, R. P. (2014). Global patterns of mesoscale eddy properties and diffusivities. *Journal of Physical Oceanography*, *44*(3), 1030–1046.

Leroux, S., Penduff, T., Bessières, L., Molines, J.-M., Brankart, J.-M., Sérazin, G., ... Terray, L. (2018). Intrinsic and atmospherically forced variability of the amoc: insights from a large-ensemble ocean hindcast. *Journal of Climate*, *31*(3), 1183–1203.

Lévy, M., Klein, P., Tréguier, A.-M., Iovino, D., Madec, G., Masson, S., & Takahashi, K. (2010). Modifications of gyre circulation by sub-mesoscale physics. *Ocean Modelling*, *34*(1-2), 1–15.

Lévy, M., Resplandy, L., Klein, P., Capet, X., Iovino, D., & Éthé, C. (2012). Grid degradation of submesoscale resolving ocean models: Benefits for offline passive tracer transport. *Ocean Modelling*, *48*, 1–9.

Maddison, J., Marshall, D., & Shipton, J. (2015). On the dynamical influence of ocean eddy potential vorticity fluxes. *Ocean Modelling*, *92*, 169–182.

Maddison, J. R., & Marshall, D. P. (2013). The eliassen–palm flux tensor. *Journal of Fluid Mechanics*, *729*, 69–102.

Mak, J., Maddison, J. R., Marshall, D. P., & Munday, D. R. (2018). Implementation of a geometrically informed and energetically constrained mesoscale eddy parameterization in an ocean circulation model. *Journal of Physical Oceanography*, *48*(10), 2363–2382.

Marshall, D. P., Maddison, J. R., & Berloff, P. S. (2012). A framework for parameterizing eddy potential vorticity fluxes. *Journal of Physical Oceanography*, *42*(4), 539–557.

Marshall, D. P., Williams, R. G., & Lee, M.-M. (1999). The relation between eddy-induced transport and isopycnic gradients of potential vorticity. *Journal of physical oceanography*, *29*(7), 1571–1578.

Marshall, J., Hill, C., Perelman, L., & Adcroft, A. (1997). Hydrostatic, quasi-hydrostatic, and nonhydrostatic ocean modeling. *Journal of Geophysical Research: Oceans*, *102*(C3), 5733-5752.

Marshall, J., Shuckburgh, E., Jones, H., & Hill, C. (2006). Estimates and implications of surface eddy diffusivity in the southern ocean derived from tracer transport. *Journal of physical oceanography*, *36*(9), 1806–1821.

McDougall, T. J. (2003). Potential enthalpy: A conservative oceanic variable for evaluating heat content and heat fluxes. *Journal of Physical Oceanography*, *33*(5), 945–963.

McDougall, T. J., & McIntosh, P. C. (2001). The temporal-residual-mean velocity. part ii: Isopycnal interpretation and the tracer and momentum equations. *Journal of Physical Oceanography*, *31*(5), 1222–1246.

Molines, J.-M., Barnier, B., Penduff, T., Treguier, A., & Le Sommer, J. (2014). Orca12. l46 climatological and interannual simulations forced with dfs4. 4: Gjm02 and mjm88. drakkar group experiment rep. tech. rep. In *Gdri-drakkar-2014-03-19* (p. 50). Retrieved from `http://www.drakkar-ocean.eu/publications/reports/orca12referenceexperiments2014`

Naveira Garabato, A. C., MacGilchrist, G. A., Brown, P. J., Evans, D. G., Meijers, A. J., & Zika, J. D. (2017). High-latitude ocean ventilation and its role in earth's climate transitions. *Philosophical Transactions of the Royal Society A: Mathematical, Physical and Engineering Sciences*, *375*(2102), 20160324.

Perezhogin, P. (2019). Deterministic and stochastic parameterizations of kinetic energy backscatter in the nemo ocean model in double-gyre configuration. In *Iop conference series: Earth and environmental science* (Vol. 386, p. 012025).

Plumb, R., & Mahlman, J. (1987). The zonally averaged transport characteristics of the gfdl general circulation/transport model. *Journal of the atmospheric sciences*, *44*(2), 298–327.

Poulsen, M. B., Jochum, M., Maddison, J. R., Marshall, D. P., & Nuterman, R. (2019). A geometric interpretation of southern ocean eddy form stress. *Journal of Physical Oceanography*, *49*(10), 2553–2570.

Redi, M. H. (1982). Oceanic isopycnal mixing by coordinate rotation. *Journal of Physical Oceanography*, *12*(10), 1154–1158.

Renault, L., Molemaker, M. J., Gula, J., Masson, S., & McWilliams, J. C. (2016). Control and stabilization of the gulf stream by oceanic current interaction with the atmosphere. *Journal of Physical Oceanography*, *46*(11), 3439–3453.

Ringler, T., Saenz, J. A., Wolfram, P. J., & Van Roekel, L. (2017). A thickness-weighted average perspective of force balance in an idealized circumpolar current. *Journal of Physical Oceanography*, *47*(2), 285–302.

Sasaki, H., Klein, P., Qiu, B., & Sasai, Y. (2014). Impact of oceanic-scale interactions on the seasonal modulation of ocean dynamics by the atmosphere. *Nature communications*, *5*(1), 1–8.

Schoonover, J., Dewar, W. K., Wienders, N., & Deremble, B. (2017). Local sensitivities of the gulf stream separation. *Journal of Physical Oceanography*, *47*(2), 353–373.

Schubert, R., Jonathan, G., Greatbatch, R. J., Baschek, B., & Biastoch, A. (2020). The submesoscale kinetic energy cascade: Mesoscale absorption of submesoscale mixed-layer eddies and frontal downscale fluxes. *Journal of Physical Oceanography*. doi: 10.1175/JPO-D-19-0311.1

Sérazin, G. (2019). `xscale`*: A library of multi-dimensional signal processing tools using parallel computing.* Retrieved from `https://github.com/serazing/xscale` doi: 10.5281/zenodo.322362

Sérazin, G., Jaymond, A., Leroux, S., Penduff, T., Bessières, L., Llovel, W., … Terray, L. (2017). A global probabilistic study of the ocean heat content low-frequency variability: Atmospheric forcing versus oceanic chaos. *Geophysical Research Letters*, *44*(11), 5580–5589.

Smith, R. D., & Gent, P. R. (2004). Anisotropic gent–mcwilliams parameterization for ocean models. *Journal of Physical Oceanography*, *34*(11), 2541–2564.

Smith, S. K., & Marshall, J. (2009). Evidence for enhanced eddy mixing at middepth in the southern ocean. *Journal of Physical Oceanography*, *39*(1), 50–69.

Stainforth, D. A., Allen, M. R., Tredger, E. R., & Smith, L. A. (2007). Confidence, uncertainty and decision-support relevance in climate predictions. *Philosophical Transactions of the Royal Society A: Mathematical, Physical and Engineering Sciences*, *365*(1857), 2145–2161.

Stammer, D. (1997). Global characteristics of ocean variability estimated from regional topex/poseidon altimeter measurements. *Journal of Physical Oceanography*, *27*(8), 1743–1769.

Stanley, G. J. (2019). Neutral surface topology. *Ocean Modelling*, *138*, 88–106.

Uchida, T., Abernathey, R. P., & Smith, S. K. (2017). Seasonality of eddy kinetic energy in an eddy permitting global climate model. *Ocean Modelling*, *118*, 41–58.

Uchida, T., Balwada, D., Abernathey, R. P., McKinley, G. A., Smith, S. K., & Lévy,

M. (2019). The contribution of submesoscale over mesoscale eddy iron transport in the open southern ocean. *Journal of Advances in Modeling Earth Systems*, *11*, 3934–3958.

Uchida, T., Balwada, D., Abernathey, R. P., McKinley, G. A., Smith, S. K., & Lévy, M. (2020). Vertical eddy iron fluxes support primary production in the open southern ocean. *Nature communications*, *11*(1), 1–8.

Vallis, G. K. (2017). *Atmospheric and oceanic fluid dynamics* (2nd ed.). Cambridge University Press.

Waterman, S., & Lilly, J. M. (2015). Geometric decomposition of eddy feedbacks in barotropic systems. *Journal of Physical Oceanography*, *45*(4), 1009–1024.

Wilson, C., & Williams, R. G. (2006). When are eddy tracer fluxes directed downgradient? *Journal of physical oceanography*, *36*(2), 189–201.

Xu, Y., & Fu, L.-L. (2011). Global variability of the wavenumber spectrum of oceanic mesoscale turbulence. *Journal of physical oceanography*, *41*(4), 802–809.

Xu, Y., & Fu, L.-L. (2012). The effects of altimeter instrument noise on the estimation of the wavenumber spectrum of sea surface height. *Journal of Physical Oceanography*, *42*(12), 2229–2233.

Young, W. R. (2012). An exact thickness-weighted average formulation of the boussinesq equations. *Journal of Physical Oceanography*, *42*(5), 692–707.

Zanna, L., & Bolton, T. (2020). Data-driven equation discovery of ocean mesoscale closures. *Geophysical Research Letters*, e2020GL088376. doi: 10.1029/2020GL088376

Zhang, S., & Lin, G. (2018). Robust data-driven discovery of governing physical laws with error bars. *Proceedings of the Royal Society A: Mathematical, Physical and Engineering Sciences*, *474*(2217), 20180305.

Zhao, K., & Marshall, D. P. (2020). Ocean eddy energy budget and parameterization in the north atlantic. In *Ocean sciences meeting 2020.*